



Eur. Phys. J. E (2019) 42: 34

DOI 10.1140/epje/i2019-11795-9

The influences of "gas" viscosity on water entry of hydrophobic spheres

Feng-Chao Yang, Xiao-Peng Chen and Pengtao Yue







Regular Article

The influences of "gas" viscosity on water entry of hydrophobic spheres

Feng-Chao Yang¹, Xiao-Peng Chen^{1,2,a}, and Pengtao Yue³

- School of Mechanics, Civil Engineering and Architecture, Northwestern Polytechnical University, Xi'an, Shaanxi, 710129, China
- ² School of Marine Science and Technology, Northwestern Polytechnical University, Xi'an, Shaanxi, 710072, China
- ³ Department of Mathematics, Virginia Polytechnic Institute and State University, Blacksburg, VA 24061-0123, USA

Received 11 October 2018 and Received in final form 22 January 2019 Published online: 21 March 2019

© EDP Sciences / Società Italiana di Fisica / Springer-Verlag GmbH Germany, part of Springer Nature,

Abstract. An extremely thin gas film was found between a sphere and a free surface when the sphere impacted onto a water pool. That might influence the generation and evolution of water entry cavity. However, it is quite difficult to be captured through normal numerical and experimental tests. In this work, by using a finite element method we investigate the water entry of a hydrophobic sphere with gas viscosity artificially increased. The air film rupture in the early stage, contact line dynamics on a curved solid surface, and air pocket formation are investigated. The numerical results reveal that the lifetime of the gas film can be predicted by a viscous squeezing flow model qualitatively well. That relates to the fact that the gas film is much thinner than the diameter of the sphere, even when the gas viscosity is 100 times as large as the liquid one. However, inviscid flow can be found in the most part of the liquid bulk. The free surface profile (or the gas film profile) is then determined by the impact speed, namely the Weber number. More importantly, after the "gas" film ruptures at the bottom of the sphere, a contact line is generated. The contact line retracts along the sphere's surface, and the retracting speed fulfils $U_{MCL} \propto T^{-1/2}$ law generally. This implies that the retracting process of the gas film is dominated by the inertia-capillary balance, rather than simply by the visco-capillary.

1 Introduction

Solid-liquid impact phenomena have attracted plenty of interests from scientific and industrial societies. They are highly nonlinear, multidisciplinary, and mainly relate to the fundamentals of wetting dynamics, gas-liquid interface evolution and coupling between micro- and macroscopic flows, etc. In nature, stone skipping over water surface, walking of animals over pool surfaces also reflect the mechanism of solid-liquid impact. The air cavity formed by the vertical entry of a sphere into water was first investigated by Worthington and Cole [1,2]. Subsequently, a series of studies were performed by May et al. [3,4]. Modern techniques of high-speed imaging further reveal the details of water entry processes, through which inviscid models are well established from the pure hydrodynamic viewpoint. Duclaux et al. [5], Aristoff and Bush [6] analysed the evolution of the air cavities as different models entered water pool, and the Rayleigh-Besant equation was demonstrated to be precise to predict the cavity dynamics.

An interesting observation was presented by Duez et al. [7] recently, who found that the wettability of the sphere did influence the occurrence of a water entry cavity. They proposed that the cavity will occur if the entering speed of the sphere is larger than a critical wetting speed, which corresponds to the wetting failure condition. This critical speed implies a visco-capillary flow in the vicinity of the moving contact line: $V_{crit} \propto f(\theta)\sigma/\mu$, where θ , σ and μ denote intrinsic contact angle, interfacial tension and viscosity, respectively. Further, Zhao and Chen [8] conducted water entry experiments for rough spheres. They proposed that air could be easily entrapped in the microscopic valleys on a hydrophilic sphere surface during the dynamic process, if the sphere is rough. Therefore, the static contact angle used in Duez's model should be replaced by a modified one, which fulfils the Cassie-Baxter model [9]. Zhao's model predicts an enhanced wetting failure for rough spheres and agrees with the experimental results very well. The usualness of the Cassie-Baxter state was further demonstrated by numerical simulations [10]. On the other hand, Ding et al. [11] conducted numerical simulations on the water entry of

a e-mail: xchen76@nwpu.edu.cn (corresponding author)

a sphere. They found that the contact line always stops on the equator of the sphere as cavity occurs. They argued that the balance between the viscous stress and Laplace pressure leads to the pinning of the contact line, which further induces the cavity.

Numerical simulations are widely applied in the relative studies, such as on the explorations of wettability effects [11–13], cavity dynamics [5,6,14], and projectile responses to the impact [15,16]. However, there are still severe limitations on resolving the contact line dynamics in numerical simulations, due to the spatial and temporal resolutions. As a matter of fact, a subtle process was found on the early stage of water entry of a sphere. Marston et al. [17] found a thin gas film is entrapped under the sphere, where the viscous effect comes into the problem. On the other hand, gas film effects can also be found in a liquid drop impacting onto a quiescent liquid surface [18,19] or onto a flat solid surface [20,21]. Unfortunately, it is missing in both Ding's [11] and Duez's [7] work. We believe there is strong connection between drop-plate impact and water entry of spheres in the sense of the contact line mo-

In our work, we will focus on the early stage of the water entry of a hydrophobic sphere through numerical simulations. Of course, we also have the technical barrier mentioned above, which makes the smallest resolvable flow structure be limited by the thickness of the liquid-gas interface. To circumvent this difficulty, we use artificially increased gas viscosities and keep the other quantities in a reasonable range. It results in a clear gas film between the sphere and the liquid surface before the gas film ruptures, while certain mechanism of contact line motion can be still reflected. This setup is slightly similar to what was adopted by Tan et al. [22], who investigated a sphere penetrating a stratified two-layer system of immiscible liquids.

2 Methodology

2.1 Numerical methods

Following Yue et al. [23–25], a diffused interface method coupling the Cahn-Hilliard (C-H) equation and Navier-Stokes (N-S) equations is adopted to capture the liquidair interface. It is demonstrated that the method is able to regularize the stress singularity on the moving contact line [26]. In this model, the liquid-air interface is diffusive (with limited thickness), but should be thin enough in an accurate simulation. The fluid properties vary continuously, but steeply, across the interface.

The N-S and C-H equations are, respectively, as follows:

$$\nabla \cdot \boldsymbol{v} = 0,$$

$$\rho \left(\frac{\partial \boldsymbol{v}}{\partial t} + \boldsymbol{v} \cdot \nabla \boldsymbol{v} \right) =$$
(1)

$$-\nabla p + \nabla \cdot \left[\mu \left(\nabla \boldsymbol{v} + (\nabla \boldsymbol{v})^T \right) \right] + G \nabla \phi - \rho \boldsymbol{g}, \tag{2}$$

$$\frac{\partial \phi}{\partial t} + \boldsymbol{v} \cdot \nabla \phi = \nabla \cdot (\gamma \nabla G). \tag{3}$$

The third equation (the convective C-H equation) describes the evolution of a phase index $(-1 \le \phi \le 1)$, of which the contours indicate the interface between two phases (normally on $\phi = 0$ level). In this work, $\phi = 1$ represents the liquid phase, and $\phi = -1$ the gas phase. Across the interface, the profile of ϕ is of hyperbolictangent [23]. This equation satisfies the general thermodynamic fundamentals, where the phase transition (diffusive flux) is controlled by the gradient of the chemical potential ∇G . The chemical potential is expressed as $G = \lambda [-\nabla^2 \phi + (\phi^2 - 1)\phi/\varepsilon^2]$. The numerical interface thickness is usually 4–8 times as large as ε (namely the capillary width), and λ denotes the mixing energy density. Both of them determine the liquid-gas interfacial tension $\sigma = \frac{2\sqrt{2}}{3} \frac{\lambda}{\epsilon}$ [23]. In the C-H equation, γ denotes mobility, which is a material constant. By neglecting convection, namely v = 0, one can see that the relaxation of the ϕ distribution depends on γ .

In the momentum equation, eq. (2), the interfacial tension is introduced as $\mathbf{F}_S = G\nabla \phi$. The symbols in eqs. (1) and (2), such as ρ and \mathbf{v} , are defined as usual, and locally averaged ones are adopted in the equations:

$$\rho = \rho_l \frac{1+\phi}{2} + \rho_g \frac{1-\phi}{2} ,$$

$$\mu = \mu_l \frac{1+\phi}{2} + \mu_g \frac{1-\phi}{2} .$$

In the expressions, the subscripts l and g represent liquid and gas, respectively. ρ_l , ρ_g , μ_l and μ_g are predefined material properties. The last term in eq. (2) represents the gravitational force, which is ignored in some of our simulations. That roots in the fact that the impact is very fast, since the speed of the sphere is nearly constant before the cavity is closed [6,27]. Our computational domain can be reasonably fixed on the "falling" sphere. On the other hand, the compressibility of the liquid could be important at the very beginning of the water impact of a blunt body [28]. However, the supersonic stage is extremely short compared to the later film generation and developing processes, so we use the incompressible fluid assumption (see eq. (1)) [29,30].

On the surface of the solid sphere, non-penetrating and no-slip conditions are applied:

$$\mathbf{v}|_{r=R} = 0, \tag{4}$$

$$\mathbf{n} \cdot \nabla G|_{r=R} = 0, \tag{5}$$

where R represents the radius of the sphere. The wetting condition is written as

$$\lambda \mathbf{n} \cdot \nabla \phi + f_w'(\phi) = 0. \tag{6}$$

n denotes the normal (outward) of the surface of the sphere, and f_w the local surface energy density. f_w relates to the static contact θ_S through the expression

$$f_w(\phi) = -\sigma \cos \theta_S \frac{\phi(3-\phi^2)}{4} + \frac{\sigma_{w1} + \sigma_{w2}}{2}.$$

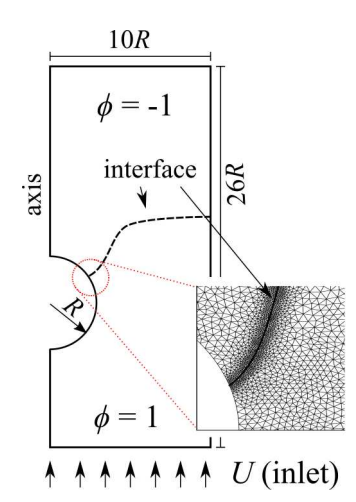


Fig. 1. The schematic of a typical computational domain, where the impact of a sphere onto a liquid surface is simulated. The radius of the sphere is R, and the size of the domain is $10R \times 26R$. The dashed line represents the liquid-gas interface, corresponding to $\phi=0$ level. The region with $\phi=1$ denotes the liquid phase, and $\phi=-1$ the gas phase. The frame is fixed on the sphere. Therefore, the velocity boundary condition with amplitude U is imposed on the lower side of the domain. The left side is the axisymmetric axis, and the other sides are set as open boundaries. The inset shows a grid distribution near the contact line.

Here, σ_{w1} and σ_{w2} represent the liquid-solid and gassolid interfacial tensions, respectively. The relation satisfies Young's equation:

$$\sigma_{w1} - \sigma_{w2} = \sigma \cos \theta_S. \tag{7}$$

The above method was validated carefully in our previous work [10], and the readers are suggested to refer to it for details.

The standard Galerkin formalism is adopted to discretize the governing equations and the boundary conditions. Specifically, the fourth-order C-H equation is decomposed into two second-order equations ahead of the discretization. An implicit scheme is used for discretization, and the resulting nonlinear system is solved by using Newton's method with a small tolerance 10^{-7} . To ensure sufficient temporal accuracy, the time step is chosen to be 0.002 initially and is gradually increased to 0.05 for all simulations. It should be noted that our numerical method is implicit and is not subject to the constraint of the CFL condition. For more details on the numerical method and convergence tests, the readers are referred to refs. [10] and [23,24].

2.2 Numerical setup

A schematic diagram of the computational domain is depicted in fig. 1. As aforementioned in sect. 2.1, our numerical domain is fixed on the sphere and we impose a uniform velocity boundary condition on the inlet. The dynamics of the impacting process is simulated in a two-dimensional

axisymmetric domain, the size of which is $26R \times 10R$. Open boundaries are imposed on the right and upper sides. That makes the water entry cavity develop fully with negligible influences from the boundaries. The inlet velocity U is set according to the impacting speed (-U).

According to refs. [24] and [25], it is required that the numerical interface should be thin enough to get accurate simulations, namely sharp interface limit. It can be expressed as $\varepsilon \leq 4l_D$, where $l_D = (\gamma \mu^*)^{1/2}$ is a diffusive slip length, and $\mu^* = \sqrt{\mu_g \mu_l}$. In the simulations, we take $\gamma = 8 \times 10^{-4}$ and $\mu^* = 0.014$ –1.0 (non-dimensionalized based on liquid density, liquid viscosiy, and sphere diameter). This requires $\varepsilon < 0.013$. To achieve the sharp interface limit, a self-adaptive mesh, implemented by Gmsh [31], is utilized in the present study. The grid size is set as 0.1R in the $\phi = \pm 1$ region, and refined gradually to 0.005R in the interfacial region (see the inset of fig. 1). Furthermore, we remesh the computational domain, if the $\phi = 0$ level set moves over a distance of $\varepsilon (= 0.01)$, and then map all the variables from the old mesh to the new one by using a least squares projection.

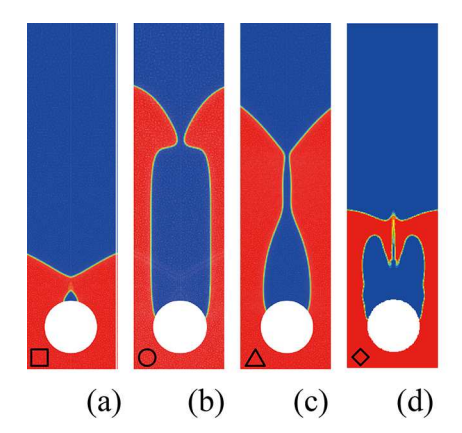
3 Results and discussions

3.1 General descriptions and validation of the methods

According to the dimensional analysis, three dimensionless numbers will influence the water entry process of a sphere, which are the Bond number $(Bo = \frac{\rho_l g R^2}{\sigma})$, the Reynolds number $(Re = \frac{\rho_l U R}{\mu_l})$ and the Weber number $(We = \frac{\rho_l U^2 R}{\sigma})$, respectively. Concerning the flow conditions widely reported in the previous studies, large Reynolds numbers are utilized in the present study, implying the viscous effects can be neglected. For hydrophobic spheres, four distinct water entry cavity profiles (water entry modes) are observed [6], including quasi-static, shallow seal, deep seal and surface seal modes, when the Bo number is not very large. Furthermore, dimensionless variables are utilized in this paper.

We first validate our numerical methods by simulating the water entry processes, with the density ratio $\lambda_{\rho} = \rho_g/\rho_l = 0.02$, and viscosity ratio $\lambda_{\mu} = \mu_g/\mu_l = 0.02$, respectively, while the other paramters are listed in table 1. Figures 2(a)–(d) show the typical free surface profiles of the various water entry modes. Figure 2(e) shows the phase diagram of the water entry modes in the Bo-We plane. According to the comparisons with the experimental measurements [6], our method can reproduce the experiments very well. It should be noted that, although our density and viscosity ratios are larger than real ones in the experiments, correct results can be obtained.

When we concern the early stage of water entry, gravity can be neglected [6,11]. The case with the dimensionless groups of We=90, Re=1500 and Bo=0 is studied for further validation. In such a circumstance, the cavity will not pinch off, and the flow is almost inviscid. Following Ding's analysis [11], the governing equation is presented



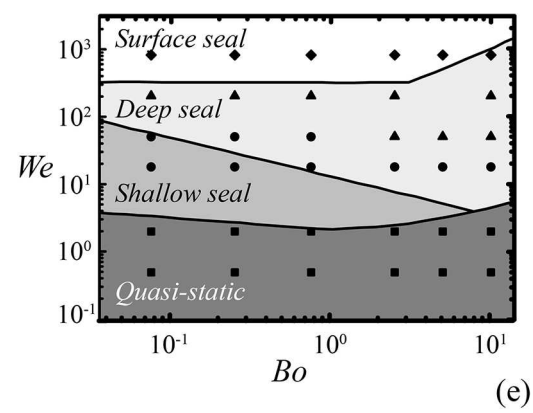


Fig. 2. Four different water entry modes according to the free surface profile: (a) quasi-static (\square), (b) shallow seal (\bigcirc), (c) deep seal (\triangle) and (d) surface seal (\bigcirc) water entry modes. (e) Phase diagram of the water entry modes in the *Bo-We* plane. The shadowed background shows the results from ref. [6], and the symbols denote the numerical results obtained from our simulations. The static contact angle $\theta_S = 120^{\circ}$ is adopted.

Table 1. Dimensionless groups.

Dimensionless numbers	Symbols	Definitions	Magnitude
Bond number	Bo	$\rho_l g R_0^2 / \sigma$	0-100
Weber number	We	$\rho_l R_0 U^2 / \sigma$	0.5 – 800
Capillary number	Ca	$U\mu_l/\sigma$	0.1 – 1.2
Reynolds number	Re	$\rho_l U R_0/\mu_l$	$10^2 - 10^3$
Density ratio	$\lambda_{ ho}$	$ ho_g/ ho_l$	0.02
Viscosity ratio	λ_{μ}	μ_g/μ_l	0.02 – 100
Contact angle	$ heta_S$		120°

as the unsteady Bernoulli equation

$$\begin{split} \frac{\partial \Phi}{\partial t} + \frac{(R_t^C)^2}{2} &= \\ \frac{1}{We} \left(\frac{R_{zz}^C}{(1 + (R_z^C)^2)^{3/2}} - \frac{1}{R^C (1 + (R_z^C)^2)^{1/2}} \right), \end{split} \tag{8}$$

where the unknowns $R^C(z,t)$ and Φ are the radius of the cavity in the horizontal plane (shown in fig. 3) and the velocity potential $(u = \nabla \Phi)$. The subscripts t and z represent the derivatives with respect to time and vertical coordinate z, respectively. The right-hand side of the equation represents the surface tension effect, and the terms in the brackets are the local curvature of the cavity surface. In order to solve the equation, a purely radial motion is assumed, which leads to a velocity potential Φ , as

$$\Phi = \begin{cases}
R^C R_t^C \ln\left(\frac{r}{R_\infty}\right), & R^C < r < R_\infty, \\
0, & r > R_\infty,
\end{cases}$$
(9)

where r is the radial coordinate. R_{∞} is a cut-off length where the radial velocity of the liquid vanishes and it is a function of time. We assume that $\ln(R_{\infty}/R^C)$ is on the order of unity as in refs. [5,11]. Substituting expression (9)

into (8) yields the Rayleigh-Besant equation for the cavity dynamics:

$$R^{C}R_{tt}^{C} + \frac{3}{2}(R_{t}^{C})^{2} = \frac{1}{We} \left(\frac{R_{zz}^{C}}{(1 + (R_{z}^{C})^{2})^{3/2}} - \frac{1}{R^{C}(1 + (R_{z}^{C})^{2})^{1/2}} \right).$$
(10)

Ding et al. [11] transform the above unsteady partial differential equation into a boundary value problem by fixing the coordinate frame on the moving object and using the fact that $\mathrm{d}z/\mathrm{d}t = \mathrm{const}$ (note that the velocity of the sphere keeps constant during the process). Then, eq. (10) can be rewritten as

$$\begin{split} \frac{\mathrm{d}R_z^C}{\mathrm{d}R^C} &= \left(\frac{1}{R^C(1+(R_z^C)^2)^{1/2}} + \frac{3}{2}We(R_z^C)^2\right) \\ &\times \left(\frac{R_z^C}{(1+(R_z^C)^2)^{3/2}} - WeR^CR_z^C\right)^{-1}. \end{split} \tag{11}$$

Given $R^{C}(z = z_{P})$ and $R_{z}^{C}(z = z_{P})$, the ordinary differential equation (ODE) can be solved easily numerically, for instance, by using Mathematica or Matlab. The starting point P, at $(R^C(z_P), z_P)$, is some point on the interface. The challenge then turns out to be the determination of the boundary conditions, *i.e.*, where point P is. Since the viscous effects influence the interface profile near the contact line, the potential flow theory is not valid in this region. We follow Ding's procedure [11], and set "P" on the interface where the vorticity of the flow field is small enough (shown in fig. 3(b)). The values of $\mathbb{R}^{\mathbb{C}}$ and R_z^C at $z=z_P$ are measured from the numerical results, and are then used as the boundary conditions to integrate eq. (11). The choice of $(R^C(z_P), z_P)$ is insensitive, however it is suggested to be located as close as possible to the sphere's surface. The comparison of cavity shapes between the theoretical and numerical results is presented in fig. 3(a). Except in the ripple region and the boundary layer, the numerical result agrees with the theoretical one very well. In addition, the moving contact line (MCL) is

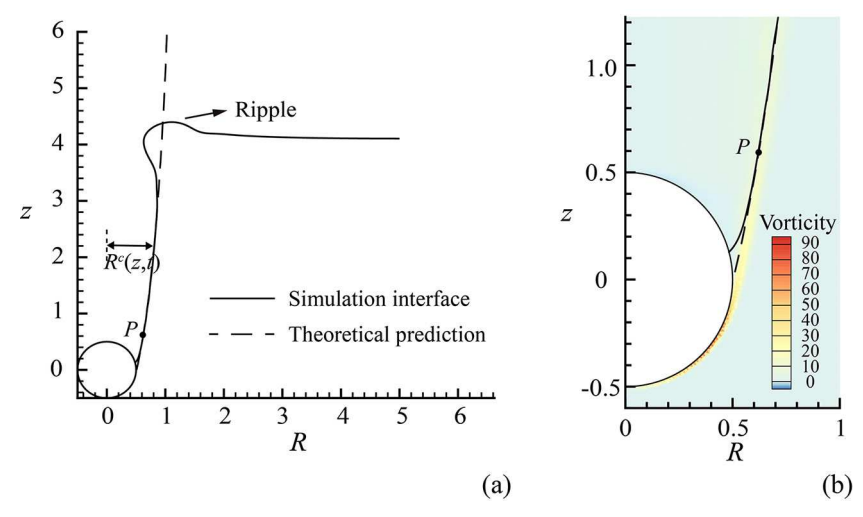


Fig. 3. (a) Comparison of cavity shapes between the simulation (solid curve) and the theoretical prediction (dashed curve) at dimensionless time T = 4.85 (the characteristic time is $T_{ref} = R/U$). We = 90, Re = 1500, Bo = 0 and $\theta_S = 120^{\circ}$, respectively. The ripple marked by an arrow shows the capillary wave propagating along the cavity surface. (b) The details of the interface profile corresponding to panel (a). The vorticity contour is included. Point P locates on the interface (z = 0.61), where the vorticity is small enough. The position and slope of the interface are measured at point P. They are applied as the boundary conditions for theoretical analysis (see eq. (11)).

pinned slightly above the equator of the sphere. This phenomenon is observed in all of our simulations when the cavity occurs.

Based on the discussions above, we can conclude that the viscous effects only play roles in a thin layer near the impacting sphere surface. Our numerical results are very consistent with the predictions of the potential theory. Meanwhile, we also note that the grid size used in the present computation is still much larger than an ideal one to resolve the details of the contact line motion. In the rest of the paper, we will discuss the early stages of the entry flow, when a hydrophobic sphere penetrates through the liquid-gas interface. The viscous effects, especially from the gas phase, will be focused on.

3.2 Lifetime of the gas film

Martson [17] argued that the gas viscosity becomes important, when the gas film between the sphere and liquid is very thin, such that a film Reynolds number $Re_f \equiv \rho_g U \delta/\mu_g \sim O(1)$, where δ is film thickness. Since our film thickness is limited by the "interface" thickness, an increased "gas" viscosity is applied. In fact, a gas film is usually entrapped below an object, when it impacts onto a liquid surface. Such object can be solid [17,19] or liquid [32]. The gas entrapment is also observed when a droplet impacts on a flat solid surface [21,20]. Those are mainly because the free surfaces are deformable. The drainage process becomes slow due to high shear stress on the solid wall.

In the simulations, we fix the other quantities and change merely the gas viscosity. The viscosity ratio λ_{μ} (= μ_g/μ_l) ranges from 0.02 to 100 (see fig. 4). This corresponds to the film Reynolds number $Re_{f,num}=10^1-10^{-2}$,

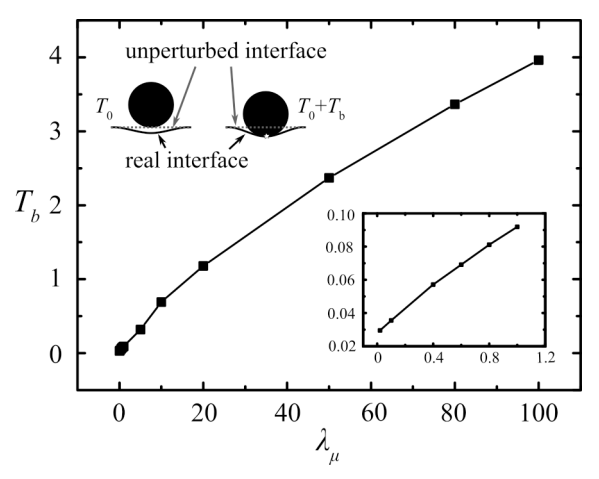


Fig. 4. Lifetime of a "gas" film (T_b) as a function of the viscosity ratio $(\lambda_{\mu} = \mu_g/\mu_l)$. The inset at the lower right corner shows the $T_b \sim \lambda_{\mu}$ relation for $\lambda = 0$ –1.0. The upper-left inset shows a sketch of the typical interface evolution before rupture and the definition of T_b .

where the film thickness is evaluated as $\delta_{num} \sim 10\varepsilon$. δ_{num} is slightly larger than the interface thickness, around $5\varepsilon - 8\varepsilon$. We then measure the lifetime of a gas film (T_b) from the numerical results with various λ_{μ} . It is defined as the time duration from the sphere bottom reaching the otherwise quiescent water surface to the film rupture (see the inset of fig. 4). After the film rupture, a MCL is generated and slips fast along the solid surface. Figure 4 shows the λ_{μ} dependence of the lifetime, which is normalized by $T_{ref} = R/U$. In the rest of the paper, dimensionless variables will be used, unless otherwise stated. U and R will be used as the characteristic velocity and length scale, respectively.

As shown in fig. 4, the lifetime increases with increasing viscosity ratio. The $T_b \sim \lambda_\mu$ relation is close to a linear one for $\lambda_\mu > 1.0$. It is worth noting that, for $\lambda_\mu < 1.0$, T_b has an order only slightly larger than 10^{-2} according to our simulations. This implies that the gas film thickness is around $(T_b \frac{R}{U}) \cdot U = T_b R \approx 10^{-2} R$. Therefore, the gas film thickness is comparable to the interface thickness (discussed in sect. 2.2). On the other hand, given a small gas density (used in the present work), an infinitesimal gas viscosity will surely lead to zero T_b , which contradicts the numerical results (see the inset in fig. 4). Therefore, we will only briefly analyse the data with $\lambda_\mu > 1.0$.

Based on the lubrication theory for squeezing flow, we assume the film is thin and the pressure is uniform over the cross-section of the film. There are two driving forces that should be considered: the dynamic pressure $p_D \sim \rho_l U^2$ and the capillary pressure $p_C \sim \sigma/R$. Since the Weber number We is much larger than unity, p_D predominates the process. As proposed in sect. 3.1, the pressure field along the free surface (below the sphere bottom) can be predicted through the potential flow theory. For various viscosity ratios, the driving forces are considered as a constant (denoted by G^* in the following analysis). The force balance in the film and the volume conservation are, respectively, expressed as

$$\frac{\mu_g u_\theta}{\delta^2} \sim \frac{\mathrm{d}p_D}{\mathrm{d}R} = G^*,\tag{12a}$$

$$u_{\theta}\delta = \mathrm{d}\delta/\mathrm{d}t.$$
 (12b)

In the equations, u_{θ} denotes the circumferential velocity, and δ the thickness of the gas film. Substituting eq. (12a) into (12b), and integrating the resultant equation, we can get $\delta \sim \sqrt{\frac{\mu_g}{G^*t}}$, i.e. $T_b \propto \mu_g$. This agrees with our numerical results qualitatively well.

Of course, the above model is very crude. A similar analysis for viscous squeezing flow can be found in ref. [33], where the relation $\delta(t) \sim t^n$ was proposed for no-slip boundaries imposed on both sides of the film. n=-0.5 is generally suggested, which is consistent with the above analysis. As a matter of fact, fig. 4 shows $T_b \propto \lambda^{0.8}$, therefore $\mu_g \propto \lambda \propto T_b^{1.25}$ and n=-0.625 according to the numerical results. The discrepancy might be because the partially slip boundary on the liquid side leads to a higher drainage rate. Of course, the deformation of the interface, pressure distribution, etc, might also influence the drainage of the film in reality [34]. The problem will be left for further investigation in the future.

3.3 Moving contact line (MCL) dynamics and interface profile

After the air film ruptures, a MCL forms and then climbs up along the surface of the sphere. We will explore the influence of gas viscosity on the MCL velocity in this section.

In fig. 5, a log-log plot of the dimensionless contact-line velocity (U_{MCL}) vs. time is presented in a wide range of viscosity ratio λ_{μ} . U_{MCL} is measured along the sphere's surface, and the time is measured after the film ruptures,

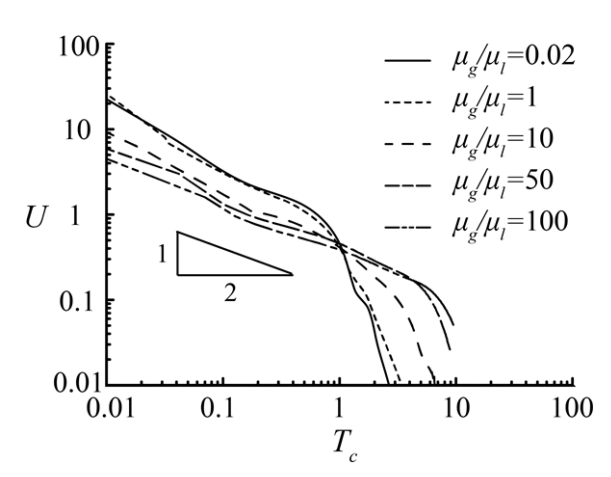


Fig. 5. The dimensionless contact-line velocity U_{MCL} along the sphere surface is plotted as a function of the dimensionless time T_c in a log-log representation. Five different viscosity ratios ($\lambda_{\mu} = \mu_g/\mu_l$) are adopted from 0.02 to 100. For all the cases, a slope of -1/2 is observed in the early stage of the film retraction. After that, the velocity decreases steeply, and the MCL is pinned near the equator of the sphere. U_{MCL} is normalized with the inlet velocity U. Time T_c is measured after the rupture of the gas film.

which is labelled as T_c . The results show that the MCL velocity meets the $U_{MCL} \propto T_c^{-1/2}$ law. If we define the circumferential position of the MCL as s_{CL} (shown in fig. 6(a)), this will fulfill the $s_{CL} \sim t^{1/2}$ law. As in fig. 5, such scaling hardly depends on λ_{μ} , although a higher viscosity does lead to a lower slipping speed. The results are consistent with Eggers's [35] and Biance's [18] findings on the initial stage of drop spreading, where the authors measured the drop spreading on a flat solid surface. That implies an inertia-capillary flow right after the rupture. After that fast advancing stage, the MCL decelerates steeply as in fig. 5. Our numerical results show that the MCL is now close to the equator of the sphere.

In Biance's analysis, a time-independent geometrical condition was utilized: $\delta(s) \propto s^2$, which is also found in our simulations (see fig. 6(b)). s denotes the curvilinear coordinate along the sphere's surface. Figure 6(a) implies that the driven-out gas accumulates slightly in a ridge at the head of the film, while the other part of the film appears almost undisturbed during the retraction process. Before the analysis, one should also note that the inertia of the "gas phase" can be neglected, although the viscosity of it is artificially increased. We then consider the motion of the liquid, which displaces the gas below the sphere (see fig. 6(a)). The mass of liquid which is entrained by the capillary force scales as $m \sim \rho s_{CL}^2 \delta \sim \rho s_{CL}^4$. During the film rupture process, the capillary energy transforms to the kinetic energy of liquid:

$$\rho s_{CL}^4 \left(\frac{\mathrm{d}s_{CL}}{\mathrm{d}t}\right)^2 \sim \sigma s_{CL}^2.$$

Therefore, we obtain

$$s_{CL}^2(t) \sim Dt, \quad D = \sqrt{\sigma/\rho}.$$

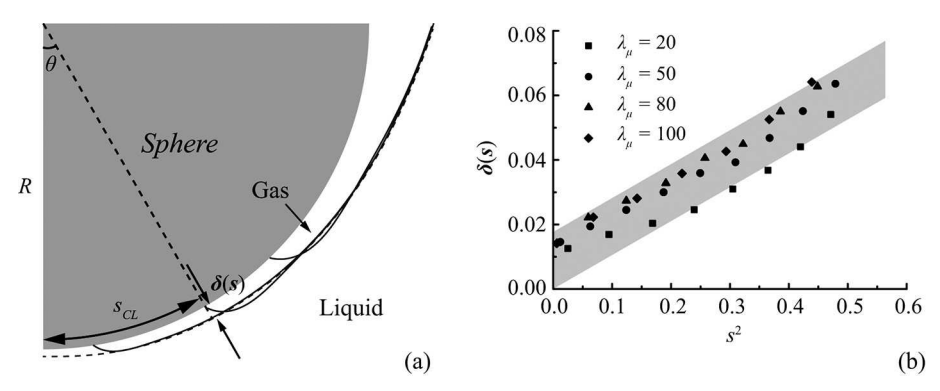


Fig. 6. (a) A schematic indicating the contact line position (s_{CL}) and the film thickness (δ) . The dashed line is presented as the interface profile before rupture. The solid curves show three snapshots of the interface during the retraction in a typical simulation. (b) δ vs. s for different λ_{μ} ranging from 20 to 100, where s denotes the curvilinear coordinate along the sphere's surface. The gray zone indicates the relation $\delta \propto s^2$.

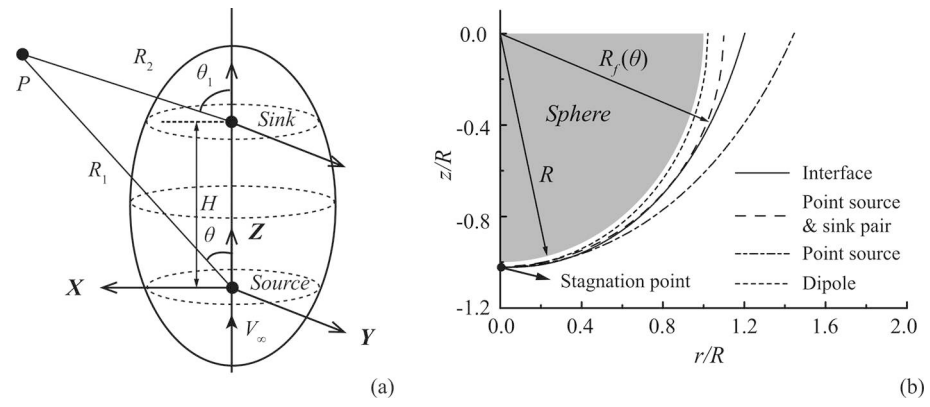


Fig. 7. (a) A sketch of the potential flow model: the influences of a point source-sink pair on uniform flow (V_{∞} at far field) in Z-direction. The sink and source have the same strength, but opposite signs. They align on the Z-axis with a distance H from each other. Concerning the axisymmetry, we only consider the flow in the X-Z plane in the context. Point P in the X-Z plane denotes a detect point, and R_1 and R_2 are the distances from the source and sink to point P, respectively. (b) The streamlines predicted through the potential flow theory and the liquid-gas interface obtained from numerical simulations (the solid curve), with We = 90, Re = 1500, $\lambda_{\mu} = 100$. The broken curves are obtained from the theoretical model: the dotted, dash-dotted and long dashed lines correspond to the dipole ($M_{dp} = Q_{dp} \cdot H|_{H\to 0} = 0.503$), point source ($Q_{src} = 0.511$) and point source-sink pair ($M = Q \cdot H = 0.655$) influences on a uniform flow, respectively. By knowing the flow in the viscous region is very slow, we suppose that the interface passes through the stagnation point marked, where a streamline passes as well.

In the analysis, we neglect the viscous effects. As pointed out by Biance [18], the $s_{CL} \sim t^{1/2}$ law is valid to a wide range of liquid viscosities, which is agreed by our results.

Although the above analysis is well demonstrated by the numerical results, the $\delta \propto s^2$ relation is not obvious. In Biance's analysis, it is obtained through the droplet profile at its bottom. In our case, the liquid-gas interface profile depends on the flow conditions and even on the interfacial tension. Thanks to the information we obtained in sect. 3.1, we know that the viscous roles should only be considered in a thin layer. Yan et al. [14] used a chain of point sources and sinks to reproduce the sphere influences on a uniform flow, where a free surface is involved. The predicted water entry cavity agrees with the experiments well. In the following part, we will show that well-distributed point source and sink do result in a correct free surface profile, which will finally lead to the $\delta \propto s^2$ relation.

As in fig. 7(a), a pair of point source and sink (we call them "disturbance" in the rest of the paper) is distributed in tandem in the flow direction. Combined with a uniform flow, the velocity potential is written as

$$\varPhi = V_{\infty} r \cos \theta - \frac{Q}{4\pi R_1} + \frac{Q}{4\pi R_2} \,, \label{eq:phi}$$

and the stream function is

$$\Psi = \frac{V_{\infty}R^2}{2}\sin^2\theta - \frac{Q}{4\pi}\left(\cos\theta - \cos\theta_2\right).$$

In these equations, Q and -Q are the strengths of the source and sink, respectively. $V_{\infty}(=U)$ denotes the uniform velocity, R_1 , R_2 and θ , θ_2 represent the distances and corresponding angles from the field point P to the point source and point sink, respectively. In the figure, the source locates on the center of the sphere, while the

position of the sink is adjustable. The distance between the source and sink is labelled as H. The above setup can be divided into three types, namely, dipole (H=0), source-sink pair (H is finite) and point source $(H\to\infty)$, depending on the distance between the source and the sink. The first type (dipole) results in the classical solution for flow around a sphere. The moment of the dipole $(M_{dp} = Q_{dp} \cdot H|_{H\to 0} = \text{const})$ can be determined by the radius of the sphere and inlet velocity (V_∞) . The last one corresponds to the point sink infinitely far from the source.

To find a reasonable configuration of the disturbances, we adjust the values of Q and H, so that a streamline (contour of Ψ) passes through the stagnation point near the head of the sphere (shown in fig. 7(b)). We also note that the profile of the streamline evolves from circle, ellipse to parabola, when H increases from zero to infinity. Figure 7(b) shows that the source-sink solution with $M = Q \cdot H = 6.55 \cdot 0.1 = 0.655$ (dashed curve) matches the simulated interface profile the best. The other two broken curves indicate typical solutions of dipole and point source in the uniform flow, respectively. Now, further concerning the geometrical expressions of a circle and ellipse in polar coordinate, and applying the polynomial expansion of $\cos \theta = 1 - (1/2!)\theta^2 + (1/4!)\theta^4 - (1/6!)\theta^6 + \cdots,$ $\delta \equiv (R_f - R) \propto \theta^2 = (s/R)^2$ can be reached on the first order (according to the contours of Ψ). In this expression, R_1 denotes the distance from a point on the elliptical streamline to the center of sphere, and R is the radius of the sphere (as in fig. 7(b)).

So far, it can be concluded that the irrotational flow leads to a certain liquid-gas interface profile ($\delta \propto s^2$). After the gas film ruptures, the capillary force drives the MCL with a velocity of $U_{MCL} \propto T_c^{-1/2}$. Compared with Maston's experiments [17], our "gas" film does not breakup into gas bubbles, which is most probably because we increase the gas viscosity, and our film is more stable. Meanwhile, the numerical simulation is limited by the spatial resolution and the interface thickness. However, our results supply some insights in the early stage contact line dynamics during water entry processes, which supplements Duez's [7] model.

4 Conclusions

We conducted a numerical study on a hydrophobic sphere penetrating through a liquid-gas interface. The early stage of the process with artificially increased gas viscosity is studied carefully. It makes the detailed flow in the "gas" film measurable, while the large scale flows are roughly the same as in the normal condition. The purpose of this study is to explore the formation of the contact line and its motion during the water entry, which is very difficult to be detected by using normal experimental and numerical methods. By noting the visco-capillary flow of the moving contact line proposed by Duez [7], our results reveal another mechanism during the occurrence of the water entry cavity: the retracting process of the contact line can be determined by the inertia-capillary balance if a thin film

with a significant area forms at impact. It is known that the wetting failure implies that the interface is nearly parallel to the solid wall at the contact line [36,37]. Therefore, our MCL should have a speed lower than Duez's prediction, *i.e.*, lower than the wetting failure velocity. Another important point is that the contact line slows down drastically when it approaches the equator of the sphere, which satisfies Ding's [11] picture.

We summarize the current results of the study as follows:

- Through the preliminary analyses and the discussions on the moving contact line motion on the sphere surface, it is found that the viscous effects play a role in a thin layer near the sphere surface, if the impact Weber number We and Reynolds number Re are large. The inviscid potential flow can be found in the bulk of the fluid, which results in the $\delta \sim s^2$ profiles of the gas film, and the water entry cavity shape can be well described by the Rayleigh-Besant equation.
- Before it ruptures, the gas film thins under the action of hydrodynamic pressure. The balance between the viscous stress and the driving force makes the lifetime of the gas film almost linearly proportional to the viscosity ratio: $T_b \propto \lambda_{\mu}$.
- After the "gas" film ruptures, the capillary force drives the gas to flow out of the film, and the contact line motion as well. With the aforementioned quadratic film thickness, the resultant contact line motion fulfils the inertia-capillary flow scenario: the contact line position on the sphere's surface evolves following $s_{CL} \sim t^{1/2}$ law. Duez's paper focuses on the contact line dynamics after the film has disappeared.

Of course, further research is still required for a deeper understanding of the water entry, including the liquid influences on the gas film drainage, the breakup modes of the gas film (3D effects), the splashing process, and so on.

The authors are grateful to Professor L.-B. Jia for insightful discussions. We also thanks to the financial support by NSFC (Grant Nos. 11472220, 11872315), and Innovation Foundation for Doctor Dissertation of NPU (Grant No. CX201516). PY acknowledges the financial support by NSF-DMS (Grant No. 1522604).

Author contribution statement

All the authors were involved in the preparation of the manuscript. All the authors have read and approved the final manuscript.

Publisher's Note The EPJ Publishers remain neutral with regard to jurisdictional claims in published maps and institutional affiliations.

References

- A.M. Worthington, R.S. Cole, Philos. Trans. R. Soc. London, Ser. A 189, 137 (1897).
- A.M. Worthington, R.S. Cole, Philos. Trans. R. Soc. London, Ser. A 194, 175 (1900).
- 3. A. May, J. Appl. Phys. 22, 1219 (1951).
- 4. A. May, J. Appl. Phys. 23, 1362 (1952).
- V. Duclaux, F. Caillé, C. Duez, C. Ybert, L. Bocquet, C. Clanet, J. Fluid Mech. 591, 1 (2007).
- 6. J. Aristoff, J.W.M. Bush, J. Fluid Mech. 619, 45 (2009).
- C. Duez, C. Ybert, C. Clanet, L. Bocquet, Nat. Phys. 3, 180 (2007).
- 8. M.H. Zhao, X.P. Chen, Q. Wang, Sci. Rep. 4, 5376 (2014).
- 9. D. Quéré, Annu. Rev. Mater. Res. 38, 71 (2008).
- F.C. Yang, X.P. Chen, P. Yue, Phys. Fluids 30, 012106 (2018).
- H. Ding, B.Q. Chen, H.R. Liu, C.Y. Zhang, P. Gao, X.Y. Lu, J. Fluid Mech. 783, 504 (2015).
- 12. M. Do-Quang, G. Amberg, Phys. Fluids 21, 022102 (2009).
- M. Do-Quang, G. Amberg, Math. Comput. Simul. 80, 1664 (2010).
- H. Yan, Y. Liu, J. Kominarczuk, D.K.P. Yue, J. Fluid Mech. 641, 441 (2009).
- 15. M. Greenhow, Appl. Ocean Res. 10, 191 (1988).
- 16. S. Gaudet, Phys. Fluids 10, 2489 (1998).
- J.O. Marston, I.U. Vakarelski, S.T. Throddsen, J. Fluid Mech. 680, 660 (2011).
- A.L. Biance, C. Clanet, D. Quéré, Phys. Rev. E 69, 016301 (2004).
- T. Tran, H. de Maleprade, C. Sun, D. Lohse, J. Fluid Mech. 726, R3 (2013).

- K. Langley, E.Q. Li, S.T. Thoroddsen, J. Fluid Mech. 813, 647 (2017).
- C. Josserand, S. Thoroddsen, Annu. Rev. Fluid Mech. 48, 365 (2016).
- B.C.W. Tan, J.H.A. Vlaskamp, P. Denissenko, P.J. Thomas, J. Fluid Mech. 790, 33 (2016).
- P. Yue, J.J. Feng, C. Liu, J. Shen, J. Fluid Mech. 515, 293 (2004).
- P. Yue, C. Zhou, J.J. Feng, C.F. Ollivier-Gooch, H.H. Hu, J. Comput. Phys. 219, 47 (2006).
- 25. P. Yue, C. Zhou, J.J. Feng, J. Fluid Mech. 645, 279 (2010).
- 26. C. Huh, S.G. Mason, J. Colloid Interface Sci. 60, 11 (1977).
- J.M. Aristoff, T.T. Truscott, A.H. Techet, J.W.M. Bush, Phys. Fluids 22, 032102 (2010).
- A.A. Korobkin, V.V. Pukhnach, Annu. Rev. Fluid Mech. 20, 159 (1998).
- 29. D. Battistin, A. Iafrati, J. Fluids Struct. 17, 643 (2003).
- 30. A. Iafrati, A.A. Korobkin, Phys. Fluids 16, 2214 (2004).
- C. Geuzaine, J.F. Remacle, Int. J. Numer. Methods Eng. 79, 1309 (2009).
- X. Chen, S. Mandre, J.J. Feng, Phys. Fluids 18, 092103 (2006).
- A.G. Petrov, I.S. Kharlamova, Eur. J. Mech. B/Fluids 48, 40 (2014).
- D.Y.C. Chan, E. Klaseboer, R. Manica, Soft Matter 7, 2235 (2011).
- J. Eggers, J.R. Lister, H.A. Stone, J. Fluid Mech. 401, 293 (1999).
- T.S. Chan, S. Srivastava, A. Marchand, B. Andreotti, L. Biferale, F. Toschi, J.H. Snoeije, Phys. Fluids 25, 074105 (2013).
- 37. M. Liu, X.P. Chen, Eur. Phys. J. E 41, 92 (2018).